
Article:
Yang, F. orcid.org/0000-0002-6428-7755, Wu, P., Du, Y. et al. (1 more author) (2024) Phase evolution, defect chemistry, and electrical properties of Na0.5Bi0.5TiO3-BiNi0.5Ti0.5O3 solid solutions. Journal of Materials Science & Technology, 196. pp. 148-161. ISSN 1005-0302

https://doi.org/10.1016/j.jmst.2024.01.050

Phase evolution, defect chemistry and electrical properties of $Na_{0.5}Bi_{0.5}TiO_3$-$BiNi_{0.5}Ti_{0.5}O_3$ solid solutions

Fan Yang[1,*], Patrick Wu[2], Yunzhu Du[1] and Derek C Sinclair[2,*]

[1] Institute of Fuel Cells, School of Mechanical Engineering, Shanghai Jiao Tong University, 800 Dongchuan Road, Minhang District, Shanghai, 200240, P. R. China.

[2] Department of Materials Science and Engineering, University of Sheffield, Sir Robert Hadfield Building, Mappin Street, Sheffield, S1 3JD, UK.

* Corresponding authors. fanyang_0123@sjtu.edu.cn; d.c.sinclair@sheffield.ac.uk

Abstract

Solid solutions of $Na_{0.5}Bi_{0.5}TiO_3$ (NBT) and $BiNi_{0.5}Ti_{0.5}O_3$ (BNiT) were prepared by a solid-state reaction route, and their electrical properties investigated by a combination of impedance spectroscopy and electromotive force measurements to explore the possibility of developing mixed ionic-electronic conductors based on NBT. Phase analysis showed that BNiT has a large solid solution limit in NBT (60% based on X-ray diffraction), and the crystal structure changes from rhombohedral to pseudo-cubic with increasing BNiT content. Neutron diffraction patterns revealed coexistence of rhombohedral and tetragonal phases when the BNiT content ≥ 40%. Electrically, incorporation of BNiT induces *p*-type electronic conduction into NBT by hopping of holes between Ni^{2+} (Ni_{Ni}^{x}) and Ni^{3+} ($Ni_{Ni}^{\cdot}$), and therefore changes the electrical conduction mechanism systematically from predominant oxide-ion conduction, to mixed ionic-electronic conduction and to predominant *p*-type electronic conduction. The total conductivity of the solid solutions showed a "V-shape" variation with increasing BNiT content. Possible mechanisms for the phase evolution and the conductivity-composition relationship were discussed. The results suggested that achieving high levels of ionic and electronic conductivity simultaneously in NBT by introducing elements with variable oxidation states remains challenging due to the competition between an enhanced electronic component and a suppressed ionic component, but a low level of BNiT incorporation is beneficial to reducing the dielectric loss of NBT for dielectric applications.

Keywords: $Na_{0.5}Bi_{0.5}TiO_3$; $BiNi_{0.5}Ti_{0.5}O_3$; oxide-ion conduction; mixed ionic-electronic conduction; phase coexistence

1. Introduction

Since the discovery of high oxide-ion conductivity in sodium bismuth titanate ($Na_{0.5}Bi_{0.5}TiO_3$, NBT) in 2014 [1], research on the electrical conductivity and conduction mechanism of NBT-based materials has been boosted. Considerable efforts have been devoted to enhancing the oxide-ion conductivity by defect chemistry engineering such as introducing low levels of Bi-deficiency [2-5] or acceptor-type dopants with fixed oxidation state on either A- or B-site [6-20]. To date, the highest bulk conductivity (σ_b) achieved in NBT-based oxide-ion conductors (~ 0.006 S cm^{-1} at 500 ºC [6]) has approached the upper limit calculated from the Nernst-Einstein equation using the physical limit for oxygen vacancy diffusivity in the perovskite lattice proposed by De Souza [21]. With high σ_b, insignificant conductivity degradation, easy densification and reasonable stability in reducing atmosphere [9], NBT-based oxide-ion conductors are considered as promising electrolyte materials for intermediate-temperature solid oxide fuel cells (IT-SOFCs) operating below 600 ºC.

As the ionic conductivity has been optimized for NBT-based oxide-ion conductors, it is interesting to explore the possibility of developing NBT-based mixed ionic-electronic conductors for potential applications as cathode materials for IT-SOFCs. Our previous study has demonstrated such possibility by incorporating transition metal Co into NBT [22]. By a comprehensive investigation on the pO_2-dependent impedance spectra of the NBT- $BiCoO_3$ solid solutions, we revealed that incorporation of $BiCoO_3$ was able to change the electrical conduction mechanism of NBT from predominant oxide-ion conduction to mixed ionic-electronic conduction. The electronic component was attributed to partial reduction of Co^{3+} to Co^{2+} caused by oxygen loss at high temperatures, which induced *n*-type electronic conduction through electron hopping between Co^{3+} (Co_{Co}^{x}) and Co^{2+} ($Co_{Co}^{\prime}$). However, as the solid solution limit of $BiCoO_3$ in NBT was found very low, i.e., 6% based on laboratory X-ray diffraction (XRD) and 4% based on scanning electron microscopy (SEM) observations, the highest conductivity obtained from the NBT-$BiCoO_3$ solid solutions was ~ 0.003 S cm^{-1}, which is not comparable to that of the state-of-the-art mixed ionic-electronic conductors for solid oxide fuel cells applications. Nevertheless, this motivates us to further explore the capacity of obtaining higher mixed conductivity in NBT-based solid solutions if a much larger concentration of transition metal ions with variable oxidation states can be introduced into NBT.

Here we select the high-pressure perovskite, $BiNi_{0.5}Ti_{0.5}O_3$ (BNiT), to form solid solutions with NBT to probe whether high level of electronic conductivity can be induced to develop a mixed ionic-electronic conductor based on NBT. The reasons for choosing BNiT are based on the following

considerations: (1) Similar to Co, Ni is a transition metal with variable oxidation states. Electronic conductivity might be induced via electron or hole hopping between Ni ions with different valences. (2) In stoichiometric NBT-BNiT solid solutions, the oxidation state of Ni should be +2. In NiO_6 octahedra, Ni^{2+} has an energetically favored electronic configuration of $t_g^6e_g^2$ [23], therefore, Ni^{2+} is in its low-spin state with an ionic radius of $r(Ni^{2+}$, 6-fold, low-spin) = 0.69 Å [24]. In other Bi-based perovskites with transition metal on the B-site such as $BiCoO_3$ and $BiFeO_3$, Co^{3+} and Fe^{3+} are stable in their high-spin states [25, 26] with ionic radii of $r(Co^{3+}$, 6-fold, high-spin) = 0.61 Å [24] and $r(Fe^{3+}$, 6-fold, high-spin) = 0.645 Å [24], respectively. Our previous studies on NBT-$BiMO_3$ (M = Al, Ga, Sc) solid solutions have shown that M with a larger ionic radius has a weaker ability to trap oxygen vacancies, and thus is beneficial to oxide-ion conduction [27, 28]. Therefore, Ni^{2+} with a larger ionic radius than Co^{3+} and Fe^{3+} may be less effective in suppressing oxide-ion conductivity of NBT, which is desirable for obtaining high mixed ionic-electronic conductivity. (3) Comparing to $BiCoO_3$, BNiT has a larger solution limit in NBT. BNiT is a high-pressure phase with orthorhombic symmetry [29, 30]. It can form solid solutions with $PbTiO_3$, $BaTiO_3$ and NBT as end members under ambient pressure [31-33]. Previously, Bai *et al.* [33] prepared phase-pure (1-x)NBT-xBNiT solid solutions with BNiT mole fraction varying between 2% and 18%. As the objective for such solid solutions is to develop ceramics with high Curie temperature (T_c) for dielectric applications, their work mainly focused on identifying two morphotropic phase boundaries (MPB) associated with the optimized piezoelectric constant (d_{33}) and strain response at x = 6 and 14%, respectively. The solid solution limit and the electrical properties of the solid solutions remain unknown, and therefore require an in-depth investigation. This will not only benefit the exploration of NBT-based mixed ionic-electronic conductors, but also provide useful information for understanding the composition-dielectric loss (tan δ) relationship in NBT-BNiT solid solutions for their dielectric applications.

In this work, $(NBT)_{1-x}(BNiT)_x$ solid solutions were prepared by a solid-state reaction method. Solid solution limit and evolution of the crystal structure with increasing BNiT content were established by XRD and neutron diffraction. Electrical conductivity and conduction mechanism were investigated by a combination of impedance spectroscopy under different atmospheres and electromotive force (EMF) measurements. Results show that incorporation of BNiT into NBT can induce co-existence of rhombohedral and tetragonal phases at room temperature in a wide composition range, and changes the electrical conduction mechanism from predominant oxide-ion conduction for NBT, to mixed ionic-electronic conduction for x = 0.2, and to predominant p-type electronic conduction for $x \geq 40\%$. However, although a high level of Ni can be introduced into NBT by forming solid solutions with

BNiT, high mixed ionic-electronic conductivity is not observed as expected. Possible reasons for phase coexistence and limited electrical conductivity enhancement were discussed.

2. Experimental

NBT-BNiT ceramics were prepared by the conventional solid-state reaction route. Na_2CO_3 (99.5%, Alfa Aesar, UK), Bi_2O_3 (99.9%, Acros organics, USA), TiO_2 (99.9%, Sigma-Aldrich, UK) and NiO (99%, Alfa Aesar, UK) were used as starting materials. The raw powders were pre-dried (300 ºC for Na_2CO_3 and Bi_2O_3, 900 ºC for TiO_2 and 600 ºC for NiO) for 8 h before weighing in appropriate quantities according to the nominal chemical formula $Na_{0.5(1-x)}Bi_{0.5(1+x)}Ti_{1-0.5x}Ni_{0.5x}O_3$ ($0 \leq x \leq 0.7$). The mixtures were ball milled in isopropanol using yttria-stabilised zirconia milling media for 6 h. After drying and sieving, the mixtures were calcined at 800 ºC for 2 h in air. The resultant powders were subjected to a second round of ball milling for 4 h, drying, sieving, calcination at 825 ºC for 2 h, and finished by another 6 h ball milling. The final powder products were compacted into green bodies using uniaxial pressing in a steel die and then isostatically pressed at 200 MPa. The green pellets were embedded in sacrificial powder of the same composition and sintered in air at 1050-1150 ºC for 2-6 h to obtain dense ceramics. After furnace-cooled to room temperature, pellets were removed from the remaining sacrificial powder and ground using SiC sand papers to obtain flat surfaces.

The crystalline phases were first examined by X-ray powder diffraction (XRD) on the polished surfaces of pellets using a Bruker D2 Phaser (Bruker, MA, USA) in a narrow 2θ range between 20 and 50º to identify the solid solution limit between NBT and BNiT. Lattice parameters were calculated from the diffraction patterns of finely ground crushed pellets using a high-resolution STOE STADI-P diffractometer (STOE & Cie GmbH, Darmstadt, Germany) operating with $CuK\alpha_1$ radiation with a linear position-sensitive detector. Data were collected in the 2θ range between 20 and 80º in steps of 0.02º, and analysed using WinXPow software (version 2.1, Darmstadt, Germany) and an internal Si standard. The XRD patterns were calibrated using a linear calibration polynomial based on the Si peaks and then refined to a pseudo-cubic cell by least-squares fittings. For selected compositions, crystal structure and phases were further investigated by powder neutron diffraction (ND) performed by the general materials diffractometer (GEM) located at the ISIS Neutron and Muon Source facility (Rutherford Appleton Laboratory, Didcot, UK). ~ 6 g finely ground powders from crushed pellets were loaded in vanadium cans. ND patterns were collected at room temperature in a vacuum chamber. Structural refinement was carried out using EXPGUI [34, 35].

Ceramic microstructure and phase purity were observed by scanning electron microscopy (SEM) on thermally etched surfaces or polished surfaces using a Philips XL30S FEG (Amsterdam, Netherland). Compositions were obtained by energy-dispersive X-ray spectroscopy (EDS) on carbon-coated polished surfaces. Oxidation states of the constituent elements were analysed by X-ray Photoelectron Spectroscopy (XPS, AXIS Ultra DLD), and peak deconvolution was carried out using CasaXPS software using a mixed Gaussian and Lorentzian function.

Electrical properties were measured by ac impedance spectroscopy. Before measurements, Au paste (T-10112, Metalor Technologies, UK) was painted to cover both surfaces of the pellets and then fired at 850 °C for 2 h to serve as electrodes. Impedance measurements were performed in air over the temperature range between 150 and 600 °C at increments of 25 °C using an Agilent E4980A impedance analyser (Agilent Technologies Inc, Palo Alto, CA) in the frequency range between 1 MHz and 20 Hz, or a Solartron Modulab system in the frequency range between 1 MHz and 0.1 Hz. For selected compositions, impedance measurements were also carried out in flowing N_2, air and O_2 at 600 °C using a Solartron 1260 system (Solartron Analytical, UK) in the frequency range between 1 MHz and 0.01 Hz. Impedance data were corrected for sample geometry and analysed using ZView software (Scribner Associates, Inc, Southern Pines, NC). Electromotive force (EMF) measurements were conducted using a ProboStat system (NorECs Norwegian Electro Ceramics AS, Oslo, Norway) to obtain the oxygen-ion transport numbers at 600, 700 and 800 °C. Detailed descriptions of the experimental setup can be found in Ref. [1]. Dielectric properties were measured using an LCR meter (Agilent E4980 Precision LCR Meter, Agilent Technologies) with an applied ac voltage of 100 mV. Data points were collected every 60 s from room temperature to 600 °C during heating using a non-inductively wound tube furnace at a ramping rate of 1 °C min^{-1}.

3. Results

3.1 Phase, microstructure and oxidation states

Fig.1 shows the XRD patterns of the sintered $(NBT)_{1-x}(BNiT)_x$ ($0 \leq x \leq 0.7$) ceramics. Single phase perovskite can be formed up to $x = 0.6$. Considerable amounts of secondary phases including $Na_{0.5}Bi_{4.5}Ti_4O_{15}$, $Bi_{12}TiO_{20}$ and NiO can be identified when x increases to 0.7. Therefore, the solid solution limit of BNiT in NBT is 60% based on XRD.

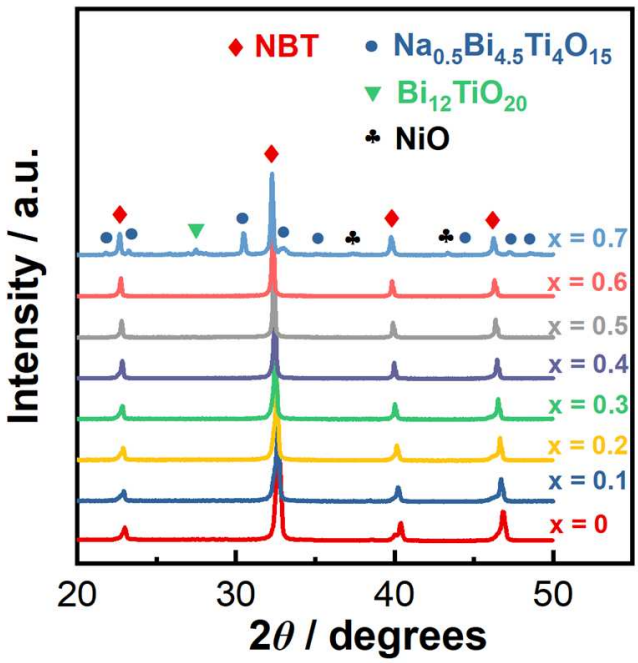

Figure 1. XRD patterns of the sintered $(NBT)_{1-x}(BNiT)_x$ ($0 \leq x \leq 0.7$) ceramics.

XRD slow scans were performed on finely ground crushed pellets of selected compositions (x = 0, 0.2, 0.4 and 0.6) to further identify the phases. The patterns in the 2θ range of 37–42° and 45.8–47.2 are presented in Fig.2a and 2b, respectively. As shown in Fig.2a, the rhombohedral distortion can be observed for x = 0 and 0.2, which gives rise to the peak broadening/splitting of the (111)p reflection and the superlattice peak at 2θ~38.5°associated with oxygen octahedral tilting [36]. Intensity of the superlattice peak is decreased when x changes from 0 to 0.2. In the 2θ range between 45.8 and 47.2° (Fig. 2b), there is no obvious splitting of the $(200)_p$ peak for all compositions. The above information suggests that the crystal structure changes from rhombohedral to pseudo cubic with increasing level of BNiT incorporation. The pseudo cubic cell volume, V, increases with increasing x, as shown in Fig.3c. A linear relationship between V and x can be established when x varies between 0 and 0.3, as indicated by the dashed line in Fig.2c. Deviation from the linear relationship occurs when $x \geq 0.4$.

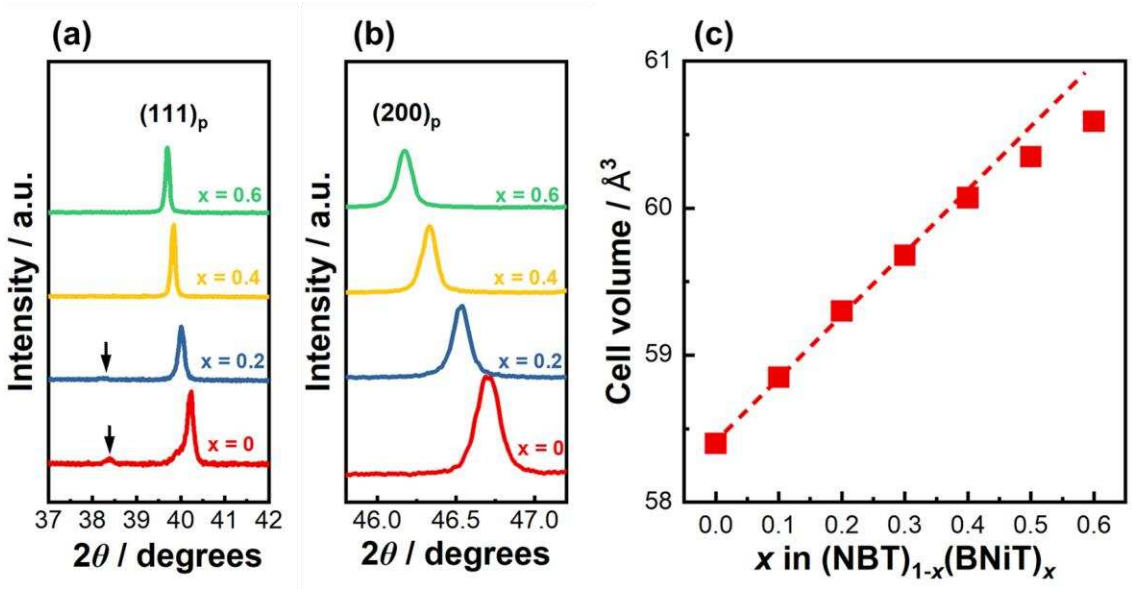

Figure 2. (a) and (b) XRD patterns of the finely ground crushed pellets in the 2θ range of 37-42° and 45.8-47.2°, respectively. The arrows in (a) indicate the superlattice peaks from the rhombohedral structure. (c) Variation of the pseudo cubic cell volume (V) as a function of x. The dashed line is the linear fitting of the V-x relationship when x varies between 0 and 0.3.

Crystalline phases of the above compositions were further investigated by powder neutron diffraction (ND). The diffraction patterns shown in Fig.3a confirm the single-phase rhombohedral structure for x = 0 and 0.2, and reveal coexistence of rhombohedral and tetragonal phases for x = 0.4 and 0.6 as evidenced by the presence of (310) and (312) diffraction peaks from the tetragonal structure (inset figure in Fig.3a). Rietveld refinements of the ND data using space group $R3c$ for x = 0 and 0.2, and $R3c$ + $P4bm$ for x = 0.4 and 0.6, show good agreement with a single rhombohedral structure for the former, and a mixture of rhombohedral and tetragonal phase for the latter, as shown by Fig.3b and 3c using x = 0.2 and 0.6 as representatives, respectively. Lattice parameters, fraction of each phase and fitting parameters are listed in Table 1, where it shows the cell volume and the weight fraction of the tetragonal phase increase with increasing x.

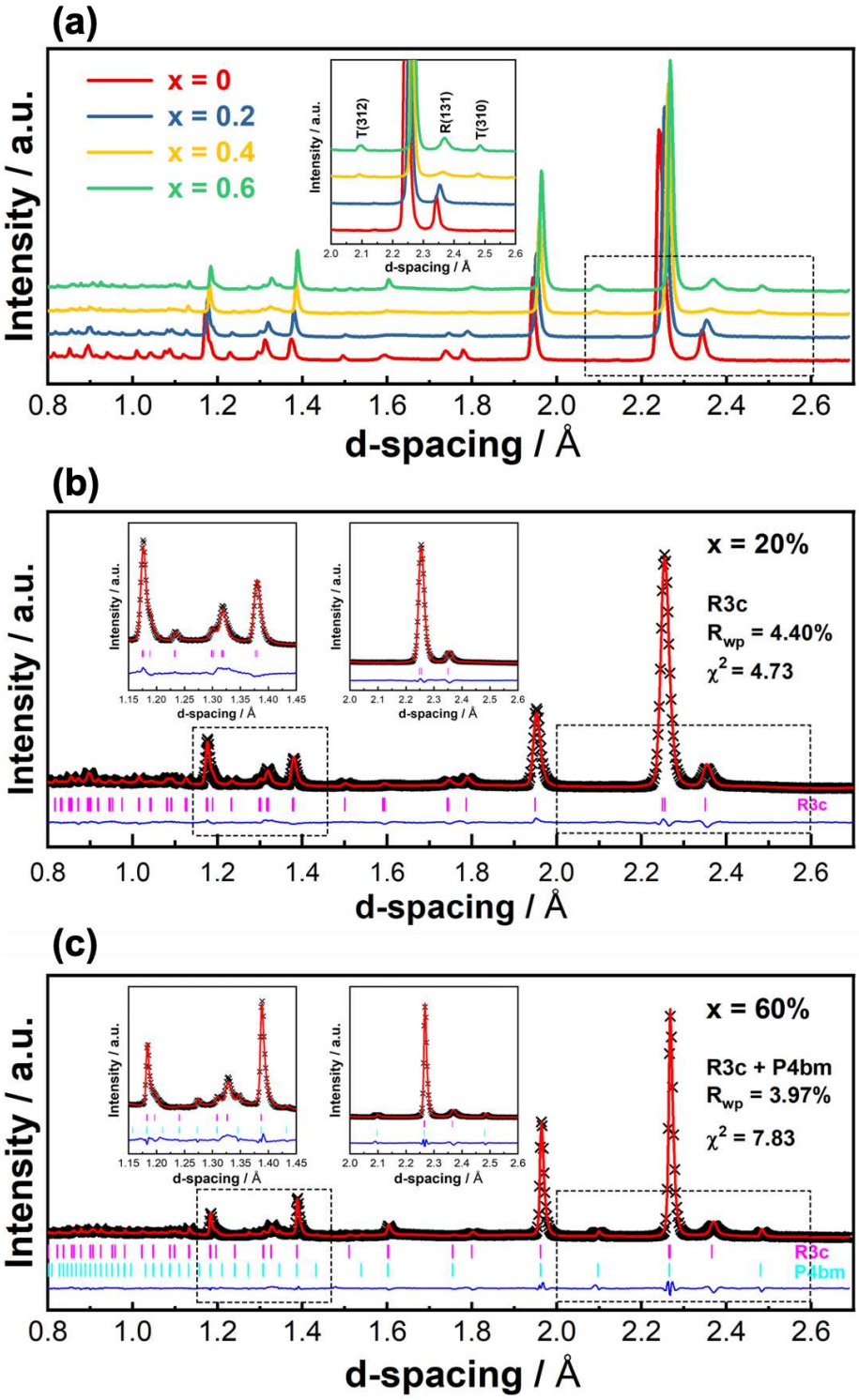

Figure 3. (a) Neutron diffraction patterns for $(NBT)_{1-x}(BNiT)_x$ (x = 0, 0.2, 0.4 and 0.6) collected at room temperature. The inset figure shows an expanded view of the *d*-spacing range between 2.0 and 2.6 Å indicated by the dashed rectangle. (b) and (c) Rietveld refinements of the ND patterns for x = 0.2 and 0.6, respectively. Cross symbols represent the observed patterns and the solid lines show the calculated fit. The reflection makers for the *R*3*c* and *P*4*bm* are shown as vertical lines with the difference patterns below. The quality of fit is indicated in each figure. The inset figures in (b) and (c)

show the expanded views of the *d*-spacing ranges of 1.15–1.45 Å and 2.0–2.6 Å in the dashed rectangles.

Table 1 Lattice parameters, relative fraction of each phase and fitting qualities from Rietveld refinement of the ND patterns

x	Space group	Lattice parameters			Fraction /%	Fitting quality	
		a / Å	c / Å	V / Å^3		χ^2	R_{wp} / %
0	R3c	5.4778	13.5091	351.054	100	4.55	4.72
0.2	R3c	5.5095	13.5339	355.783	100	4.73	4.40
0.4	R3c	5.5320	13.5830	359.989	76.28	7.12	3.94
	P4bm	5.5359	3.9164	120.022	23.72		
0.6	R3c	5.5475	13.6045	362.581	64.63	7.83	3.97
	P4bm	5.5480	3.9255	120.827	35.37		

Phase purity and compositions were further examined by SEM and EDS on polished surfaces of pellets. Clean surfaces can be observed for $x \leq 0.3$, as shown by Fig.4a using $x = 0.2$ as an example. Small amounts of secondary phases can be identified for $x \geq 0.4$, as indicated by the dashed circle in Fig.4b using $x = 0.4$ as an example. EDS analysis suggests the secondary phase is Ni-rich, as shown by the inset table in Fig.4b. Compositional analysis of the solid solutions (Fig.4c and 4d) shows that the atomic fractions of cations, both on the A-site (Na, Bi) and the B-site (Ti, Ni), are generally consistent with their expected values, which gives additional evidence for the formation of solid solutions between NBT and BNiT. SEM micrographs of the thermally-etched surfaces (Fig.5) show typical ceramic microstructures with grain sizes varying between 2 ~ 8 μm.

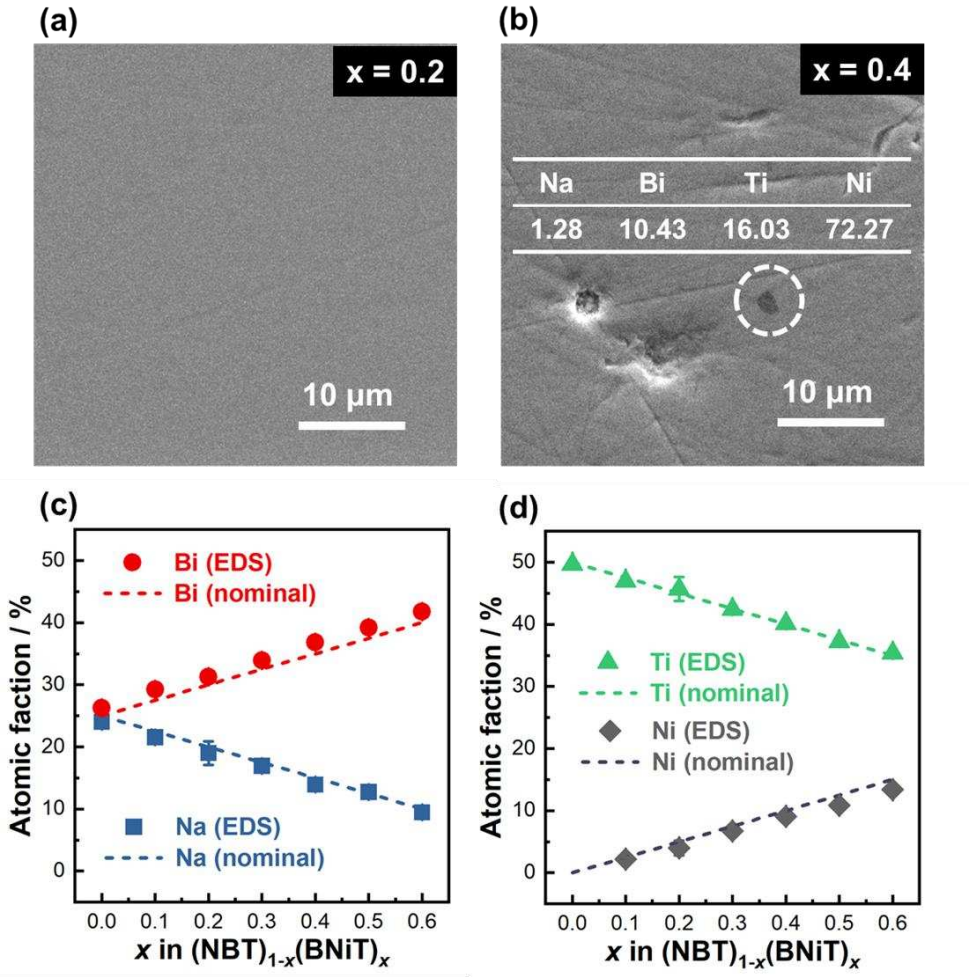

Figure 4. (a) and (b) SEM micrographs of polished surfaces of x = 0.2 and 0.4, respectively. The dashed circle in (b) indicates the presence of a Ni-rich secondary phase. The atomic fraction of each cation of the circled region is listed in the inset table. (c) and (d) Atomic fractions of the A-site (Na, Bi) and B-site (Ti, Ni) cations obtained from EDS, respectively. Data were collected from 5 randomly selected areas on polished surfaces.

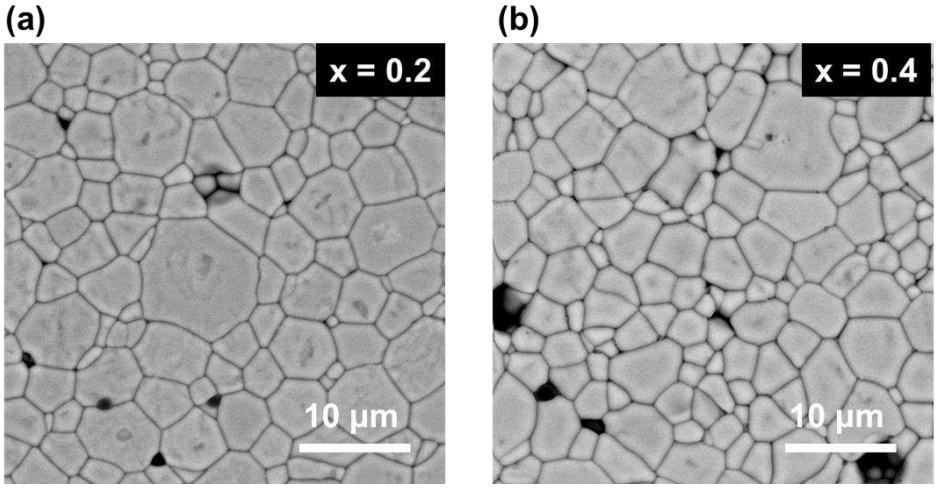

Figure 5. SEM micrographs of a thermally-etched surface of (a) x = 0.2 and (b) x = 0.4.

Chemical states of Na, Bi, Ti, Ni and O in the sintered NBT-BNiT ceramics were analysed by XPS. The survey spectrum of a selected composition, $x = 0.2$, is presented in Fig.6a. The high-resolution spectra and peak fittings of Na 1s (Fig.6b) and Bi 4f (Fig. 6c) show they are in +1 and +3 oxidation states, respectively. The Ti 2p spectrum (Fig.6d) consists of two main peaks at ~ 458 and ~ 465 eV, where the low binding energy (BE) peak at 457.82 eV corresponds to Ti $2p_{3/2}$, and the high BE region corresponds to partially overlapped peaks of Ti $2p_{1/2}$ (463.52 eV) and Bi $4d_{3/2}$ (465.04 eV). The full width at half maximum (FWHM) of the Ti $2p_{3/2}$ peak from fitting is 1.42 eV, which is smaller than that of TiO_2 and $BaTiO_3$ (1.94 and 2.0 eV, respectively [37]), suggesting the absence of Ti^{3+} ions [38]. Therefore, Ti exists in the form of Ti^{4+}. The Ni 2p region (Fig.3e) consists of four peaks, corresponding to Ni $2p_{3/2}$ and Ni $2p_{1/2}$ at 856.06 and 873.62 eV, and two characteristic shake-up satellite peaks for Ni^{2+} (referred to as 'sat.') at ~862 and ~880 eV, respectively [39]. The O 1s spectrum (Fig.6f) can be deconvoluted into four main peaks, from low to high BE, corresponding to the lattice oxygen (peak I, 529.45 eV), highly oxidative oxygen (peak II, 530.54 eV), surface oxygen/hydroxyls (peak III, 531.49 eV), and surface absorbed water (peak IV, 532.83 eV), respectively [40].

As pointed out by Bondarchuk *et al.* [41], the traditional approach to distinguish Ni^{2+} and Ni^{3+} by fitting the Ni $2p_{3/2}$ peak using two components and assigning the peaks centered at lower and higher BEs to Ni^{2+} and Ni^{3+} can be speculative as deconvolution of such symmetric peak using two components is prone to give ambiguous results. They proposed a novel method to quantify the fraction of Ni^{3+} using the ratio between the intensity of the Ni $2p_{3/2}$ peak and the shake-up satellite peak based on the assumption that Ni^{3+} species make virtually no contribution to the satellite intensity. Here we adopted this method to estimate the fraction of Ni^{3+} using the following equation:

$$f(Ni^{3+}) = \left(1 - \frac{1.3 \times I(sat.)}{I(I(Ni\ 2p_{3/2})}\right) \times 100\% \quad (1)$$

where I denotes the peak intensity obtained by peak deconvolution. The normalized peak intensity and the calculated Ni^{3+} fraction for the NBT-BNiT solid solutions are listed in Table 2, where it shows the Ni^{3+} faction varies around 40% for $x \leq 0.3$, and ~50% for $x \geq 40\%$.

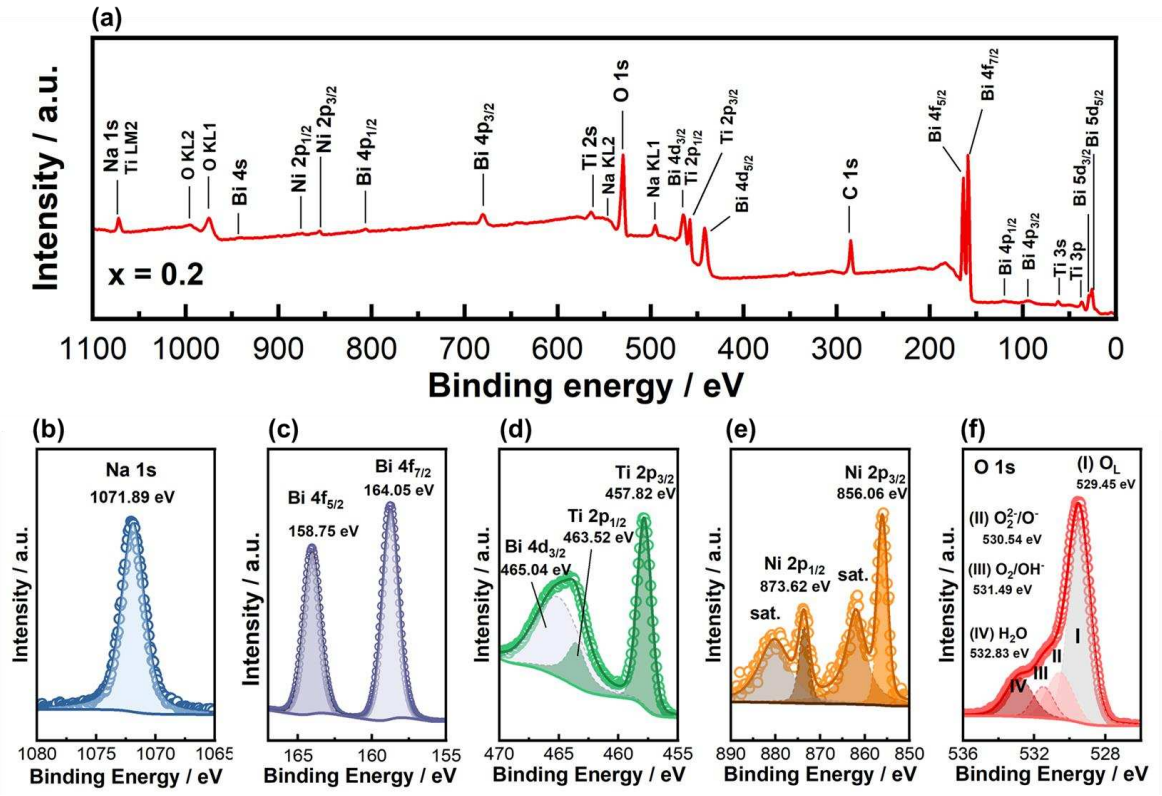

Figure 6. (a) XPS survey spectrum of $(NBT)_{1-x}(BNiT)_x$ (x = 0.2); (b)–(f) high resolution spectra and peak deconvolutions of Na 1s, Bi 4f, Ti 2p, Ni 2p and O 1s, respectively. Peaks for all elements were calibrated using C 1s.

Table 2 Ni^{3+} fraction calculated from the normalized peak intensity for Ni $2p_{3/2}$ and the shake-up satellite for the $(NBT)_{1-x}(BNiT)_x$ solid solutions.

x	Normalized peak intensity / a. u.		Ni^{3+} fraction / %
	Ni $2p_{3/2}$	Satellite	
0.1	1	0.464	39.7
0.2	1	0.497	35.4
0.3	1	0.442	42.5
0.4	1	0.361	53.0
0.5	1	0.402	47.7
0.6	1	0.399	48.2

3.2 Electrical properties

Impedance spectra for $(NBT)_{1-x}(BNiT)_x$ (x = 0, 0.2, 0.4 and 0.6) ceramics measured at 300 °C are presented in Fig.7. For NBT (x = 0), the complex plane Z^* plot (Fig.7a) is featured by a well-resolved arc at high frequency, as shown by the inset figure in Fig.7a, and a less well-resolved arc which

merges into a large tail at low frequencies. Combined Z'' and M'' spectroscopic plots (Fig.7b) show a single M'' peak centered at ~ 10 kHz, which coincides with the Z'' peak in the high-frequency region of the Z''-log$f$ plot, as shown in the inset figure of Fig.7b. The C'-log$f$ plot (Fig.7c) shows a high-frequency plateau with a C_1 value ~ 2.6×10^{-10} F·cm^{-1}, corresponding to a relative permittivity value ~ 2900, which agrees with the reported permittivity value of NBT at 300 °C [1]. A second plateau at ~ 100 Hz with a C_2 value ~ 6.6×10^{-9} F·cm^{-1}, which is more than one order of magnitude higher than C_1, agrees with the capacitance magnitude for grain boundaries (GBs) [42]. C' further increases with decreasing frequency and approaches 10^{-7} F·cm^{-1} at 1 Hz, suggesting the low-frequency response originates from the sample/electrode interface [42]. Combining the above information, the three arcs on the Z* plot, from high to low frequency, represent the responses from the bulk, GBs and electrode effect, respectively. The impedance data are therefore fitted by an equivalent circuit of three resistor-constant phase elements (R-CPE) connected in series (inset figure in Fig.7a). The capacitance values are calculated from the fitting parameters according to $C = R^{(1-n)/n}Q^{1/n}$ [43]. The resistance and capacitance values are listed in Table 3.

With BNiT incorporation, impedance spectra show different features from NBT. As shown in Fig.7d, the Z* plot for $x = 0.2$ shows two poorly-resolved arcs at high and medium frequencies, along with a third arc at low frequency. The above information can be also reflected by the Z''-log$f$ plot (Fig.7e) where two bumps at ~ 3.98 kHz and ~ 500 Hz, along with a low-frequency peak centered at 12.6 Hz, can be identified. M''-log$f$ plot, on the other hand, displays a single but asymmetric peak centered at 3.98 kHz. Coincidence of the M'' and Z'' peaks at 3.98 kHz suggests that the high-frequency response originates from the bulk. On the C'-log$f$ plot (Fig.7f), the high frequency plateau with a C_1 value ~ 1.8×10^{-10} F·cm^{-1} gives further evidence for the bulk response. The second poorly-resolved plateau with a C_2 value ~ 7×10^{-10} F·cm^{-1}, which is in the same order of magnitude with C_1. The third plateau with a C_3 value ~ 6.7×10^{-9} F·cm^{-1} agrees with the capacitance magnitude for GBs. The impedance data are fitted by an equivalent circuit of three R-CPE connected in series (inset figure in Fig.7d) to extract the resistance and capacitance values for the three responses. As also shown in Table 2, the C_2/C_1 ratio is 5.3. Therefore, the second arc can be best ascribed to a second bulk response. As $(NBT)_{0.8}(BNiT)_{0.2}$ is single phase, the second bulk response may originate from an electrical core-shell type behaviour. The core-shell structure is not obvious under SEM, suggesting the compositional deviation between the core and shell is small. C_3/C_1 ratio is ~ 43, which is close to the C_2/C_1 ratio for NBT. This gives additional evidence that the third response stems from GBs.

For $x = 0.4$, the Z^* plot displays two arcs (Fig.7g). M''-log$f$ plot shows a single peak centered at 12.6 kHz, which coincides with the Z'' peak in the high frequency region on the Z''-log$f$ plot (Fig.7h), suggesting that the high frequency response originates from the bulk. A bump at ~ 398 Hz can be observed on the Z'' spectroscopic plot. C'-log$f$ plot (Fig.7i) shows two plateaux with C_1 and C_2 values ~ 1.5 and 6.7 × 10^{-10} F·cm^{-1}, respectively. The impedance data are fitted by an equivalent circuit of two R-CPE connected in series (inset figure in Fig.7d) to extract the resistance and capacitance values. As listed in Table 2, the C_2/C_1 ratio is 43.7, which consists with the capacitance ratio between GB and bulk. Consequently, the second arc on the Z^* plot represents the GB response. When x is further increased to 0.6, the Z^* plot shows only one arc (Fig.7j). Combined Z'' and M'' spectroscopic plots (Fig.7k) show a single M'' peak centered at ~ 199.5 kHz, at which a single Z'' peak can be also observed. Coincidence of the M'' and Z'' peaks suggests that the response originates from the bulk. C'-log$f$ plot (Fig.7l) shows only one plateau, and the C' value in a magnitude of 10^{-10} F·cm^{-1} gives further evidence for the bulk response. Therefore, the impedance data are fitted by an equivalent circuit of one R-CPE, as shown by the inset figure in Fig.7j.

Impedance measurements and equivalent circuit fittings were performed at different temperatures and the total resistance, R_{total}, were extracted and converted to total conductivity, σ_{total}, according to $\sigma_{total} = 1/ R_{total} = 1/ (R_b + R_{GB})$. Arrhenius plots for σ_{total} are shown in Fig.8a, from which the activation energy, E_a, can be calculated and presented in Fig.8b. For pure NBT ($x = 0$), there is a change of E_a from 1.15 eV in the low temperature range (< 325 °C) to 0.75 eV in the high temperature range (> 325 °C). As pointed out by our previous study [44, 45], a change of activation energy for bulk conduction from ~ 0.85 eV to 0.5 eV at ~ 325 °C is a signature behaviour for ionically conducting NBT. E_a values for σ_{total} are higher than those for σ_b due to the contribution from the ionically-blocking GBs. With BNiT incorporation, the solid solutions all display linear relationship between σ_{total} and T^{-1} over a wide temperature range. E_a decreases continuously with increasing x from 1.07 eV for $x = 0.1$ to 0.4 eV for $x = 0.6$ (Fig.8b). The compositional dependence of σ_{total} at selected temperatures is shown in Fig.8c, where a V-shape variation of σ_{total} with increasing x can be observed. The lowest and highest σ_{total} values are achieved at $x = 0.1$ and 0.6, respectively. It is worth mentioning that the enhancement of σ_{total} at the solid solution limit ($x = 0.6$) is more pronounced at lower temperatures, for example, σ_{total} for $x = 0.6$ is two orders of magnitude higher than that for NBT at 300 °C, whereas less than half order of magnitude higher at 600 °C.

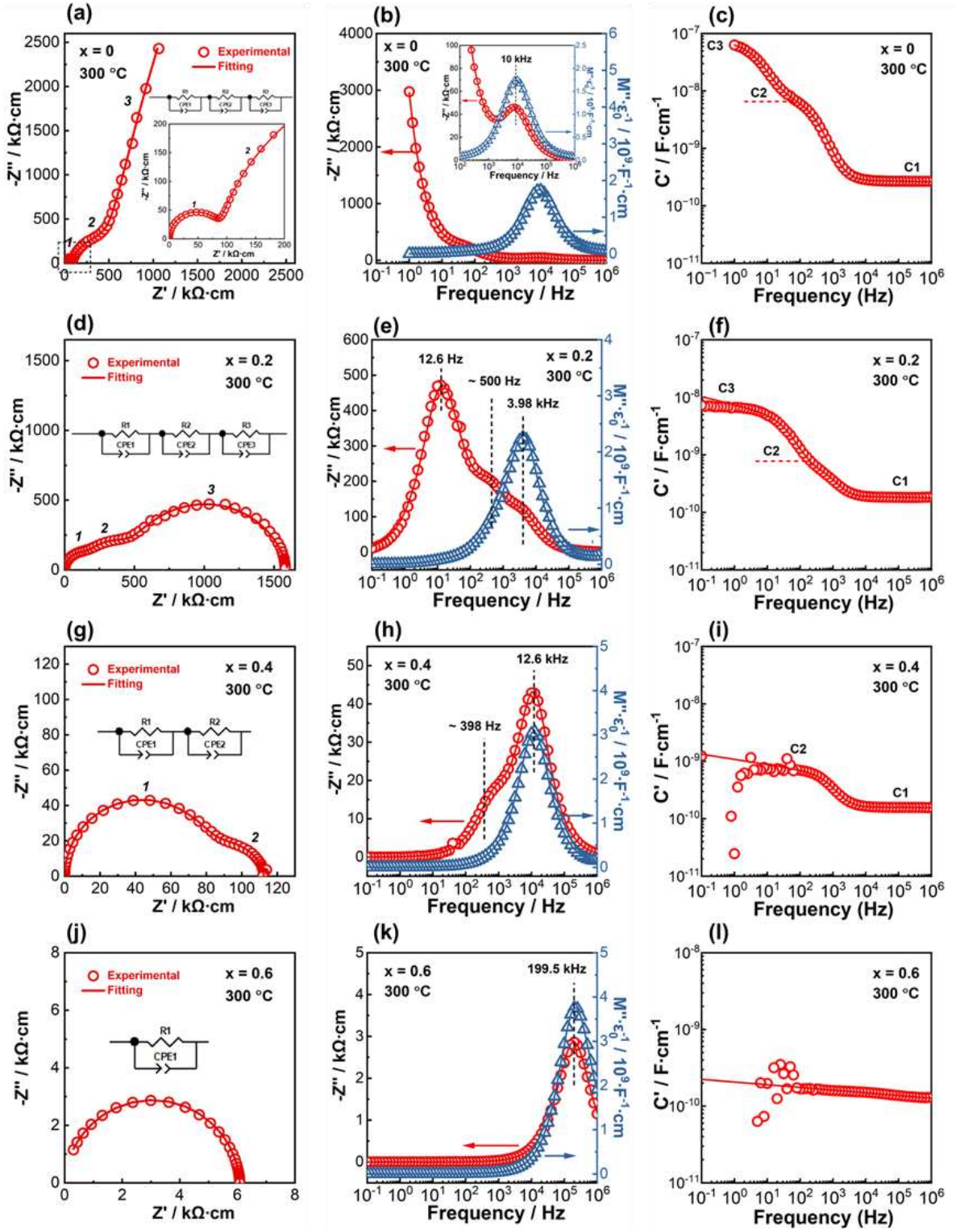

Figure 7. Impedance spectra for $(NBT)_{1-x}(BNiT)_x$ (x = 0, 0.2, 0.4 and 0.6) measured at 300 °C in air. (a), (d), (g) and (j) Z^* plots and equivalent circuits for fitting; (b), (e), (h) and (k) combined Z'' and M'' spectroscopic plots; (c), (f), (i) and (l) C' spectroscopic plots. The hollow symbols are experimental data and the solid lines are the fitting curves.

Table 3. Resistance and capacitance values obtained from equivalent circuit fitting of the impedance data at 300 °C.

x	R_1 / Ω·cm	C_1 / F·cm^{-1}	R_2 / Ω·cm	C_2 / F·cm^{-1}	R_3 / Ω·cm	C_3 / F·cm^{-1}	C_2/C_1	C_3/C_1
0	8.44×10^4	2.12×10^{-10}	3.90×10^5	9.97×10^{-9}	4.73×10^7	7.43×10^{-8}	47	350.5
0.2	1.56×10^{-9}	2.38×10^{-10}	2.95×10^5	1.27×10^{-9}	1.15×10^6	1.02×10^{-8}	5.3	42.9
0.4	8.20×10^4	1.64×10^{-10}	3.05×10^4	7.18×10^{-9}			43.7	
0.6	6082	1.35×10^{-10}						

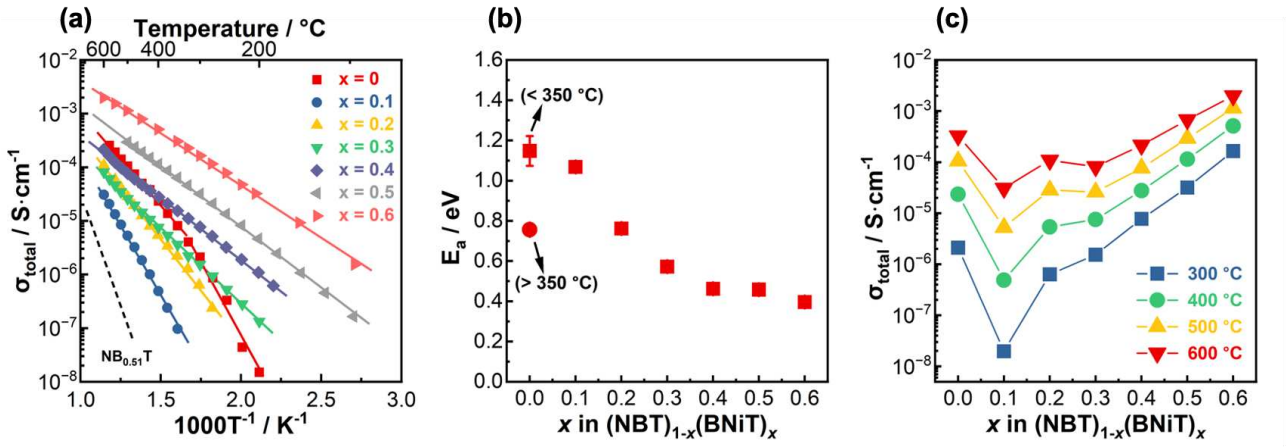

Figure 8. (a) Arrhenius plots for σ_{total}. Data for the insulating $NB_{0.51}T$ are included for comparison; (b) E_a for σ_{total} as a function of the compositional factor x; (c) Compositional dependence of σ_{total} at 300, 400 and 500 °C.

Impedance spectra measured in flowing nitrogen, air and oxygen at 600 °C over a wide frequency range between 1 MHz and 0.01 Hz are presented in Fig.9. Data for NBT can be found in our previous publication [22], thus they are not presented here. As reported previously, the bulk response for NBT is independent on atmosphere. The GB response is smallest in nitrogen (low oxygen partial pressure, pO_2) and largest in oxygen (high pO_2), showing presence of n-type electronic conduction for GBs. The low-frequency electrode spike associated with diffusion of oxygen molecules is most prominent in nitrogen and least prominent in oxygen. The oxide-ion transport number, t_{ion}, at 600 °C is 0.94 [1]. The above information suggests that the electrical conduction in NBT is predominated by oxygen ions with minor contribution from electrons. Z^* plots for $x = 0.2$ measured in different atmospheres are shown in Fig.9a. The impedance is largest in nitrogen and smallest in oxygen, suggesting the presence of p-type electronic conduction. The electrode spike can be observed at low frequencies, suggesting the presence of oxide-ion conduction. Therefore, $(NBT)_{0.98}(BNiT)_{0.2}$ shows a mixed ionic-

electronic conduction behaviour. Atmosphere tests for x = 0.4 and 0.6 also show the presence of *p*-type electronic conduction (Fig.9b and 9c). Expanded views of the low-frequency regions indicate the absence of any electrode effect (inset figures in Fig.9b and 9c), suggesting the absence of oxide-ion conduction in these compositions.

The electrical conduction mechanism is further revealed by EMF transport number measurements, and the results are presented in Fig.9d. t_{ion} values decrease with increasing x at temperatures between 600 and 800 °C, for example, t_{ion} is ~ 10% for x = 0.2, and it decreases to zero for x = 0.4 and 0.6 at 600 °C. Moreover, t_{ion} values for x = 0.2, 0.4 and 0.6 increase with increasing temperature, for example, from 10% at 600 °C to 20% at 800 °C for x = 0.2. Such variation of t_{ion} with temperature is opposite to that of NBT, which shows a lower t_{ion} at 800 °C. Combining the results from atmosphere tests and oxide-ion transport number measurements, it can be concluded that x = 0.2 shows a mixed ionic-electronic conduction mechanism with larger contribution from *p*-type electronic conduction than oxide-ion conduction. x = 0.4 and x = 0.6 show predominant *p*-type electronic conduction behaviour with minor contribution from oxygen ions. Therefore, incorporation of BNiT into NBT changes the electrical conduction mechanism from predominant oxide-ion conduction (x = 0), to mixed ionic-electronic conduction (x = 0.2), to predominant *p*-type electronic conduction (x = 0.4 and 0.6).

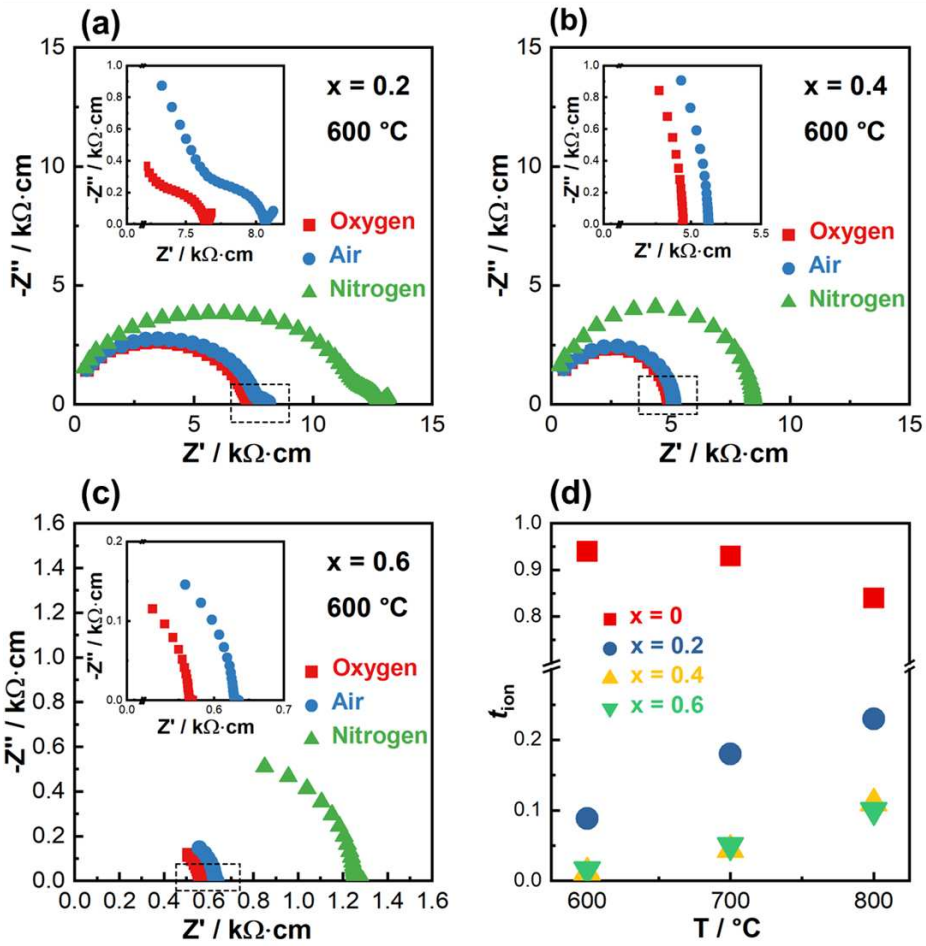

Figure 9. (a)-(c) Z* plots of $(NBT)_{1-x}(BNiT)_x$ measured at 600 °C in flowing nitrogen, air and oxygen for x = 0.2, 0.4 and 0.6, respectively. The inset figures show expanded views of the low-frequency regions indicated by the dashed rectangles. (d) Oxide-ion transport number, t_{ion}, measured at 600, 700 and 800 °C. Data for x = 0 are extracted from Ref. [1].

3.3 Dielectric properties

Permittivity–temperature (ε_r–T, 1 MHz) profiles for $(NBT)_{1-x}(BNiT)_x$ solid solutions are presented in Fig.10a. The permittivity maximum, $\varepsilon_{r,\,max}$, decreases continuously with increasing x. Peak flattening can be also observed with increasing x. For x = 0.6, a high permittivity value ~ 950 is almost temperature independent between 150 and 500 °C. The temperature for $\varepsilon_{r,\,max}$ (T_m) shows a slight increase from 323 °C for NBT to ~ 340 °C for $x \leq 0.2$, and then a dramatic drop to ~200 °C with increasing x, as indicated by the dash line in Fig.10a. Dielectric loss–temperature profile ($\tan\delta$–T, 1 MHz) shows that the temperature at which $\tan\delta$ starts to rise sharply is significantly changed by BNiT incorporation (Fig.10b). For a clear comparison, the temperature where $\tan\delta$ reaches 0.2, $T_{\tan\delta = 0.2}$, is adopted and plotted as a function of x, as shown in Fig.10c, where a 'volcano'-shape relationship

between $T_{\tan\delta = 0.2}$ and x can be observed. Furthermore, $T_{\tan\delta = 0.2}$ is negatively correlated to σ_{total} (Fig.10d), suggesting that a more rapid increase in tanδ at lower temperatures can be triggered by a higher σ_{total}, which is undesirable for dielectric applications of these solid solutions.

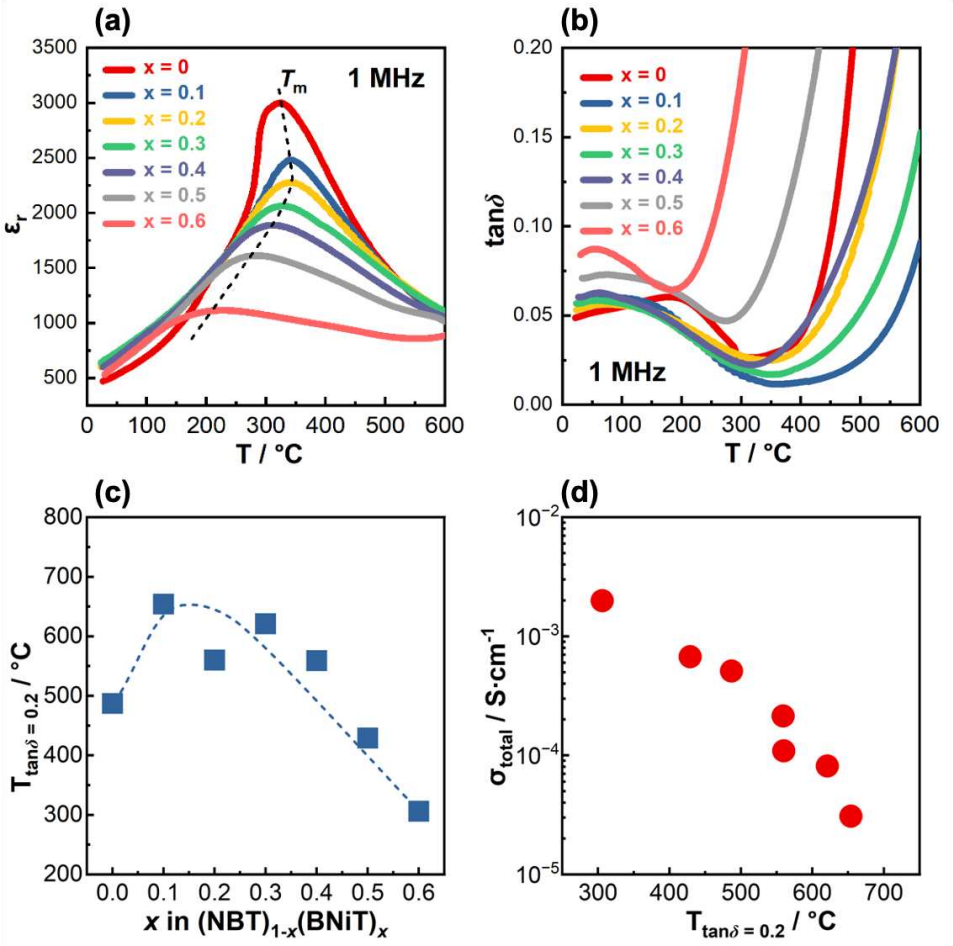

Figure 10. Dielectric properties of the $(NBT)_{1-x}(BNiT)_x$ ceramics: (a) permittivity at 1 MHz versus temperature. The dashed curve indicates the variation of T_m with x. (b) Dielectric loss (tanδ) at 1 MHz versus temperature. (c) Variation of $T_{\tan\delta = 0.2}$ with the compositional factor x. The dashed curve is a guide to the eye. (d) Relationship between σ_{total} (600 °C) and $T_{\tan\delta = 0.2}$. Data were collected during heating.

4. Discussion

The major discovery of this work is that incorporation of BNiT into NBT has a dramatic impact on its crystal structure and electrical conduction mechanism. With increasing BNiT content in the $(NBT)_{1-x}(BNiT)_x$ solid solutions, the crystal structure tends to change from rhombohedral to pseudo-cubic. Neutron diffraction patterns show coexistence of rhombohedral and tetragonal phases at room temperature for $x \geq 0.4$. On the other hand, the total electrical conductivity shows a V-shape variation

with increasing x and the conduction mechanism changes from predominant oxide-ion conduction for NBT, mixed ionic-electronic conduction for $x = 0.2$, to predominant p-type electronic conduction for $x \geq 0.4$. In the following sections, the phase evolution, in particular, the stabilisation mechanism for the tetragonal phase at room temperature, and the conductivity-composition relationship in the $(NBT)_{1-x}(BNiT)_x$ solid solutions are discussed.

4.1 Stabilisation of the tetragonal phase at room temperature

The structural stability and distortion of a perovskite (ABO_3) can be described by the Goldschmidt tolerance factor (t), $t = \frac{r_A + r_O}{\sqrt{2}(r_B + r_O)}$, where r_A and r_B represent the ionic radii of the 12-fold coordinated A-site cation(s) and the 6-fold coordinated B-site cation(s), respectively; r_O is the ionic radius of the 6-fold coordinated oxygen anion (r_O = 1.40 Å [24]). Stable perovskite compounds can be formed when t varies in a wide range between 0.75 and 1.05 [46]. An ideal cubic perovskite structure with corner-sharing rigid BO_6 octahedra is expected to be present when $t = 1$ [47]. Deviation of t from unity results in octahedral distortions (including tilting and rotating) to lower the structure symmetry [48].

BNiT has a tolerance factor (t = 0.9498) [33], which is lower than that of NBT (t = 0.9841 [27]). Therefore, incorporation of BNiT into NBT decreases t, which should lead to the formation of a lower symmetry phase such as rhombohedral, orthorhombic or monoclinic phase. However, XRD patterns show the symmetry of the $(NBT)_{1-x}(BNiT)_x$ solid solution tends to become pseudo-cubic with increasing x. An enhanced symmetry with increasing x is confirmed by ND patterns that the high-temperature tetragonal phase of NBT is stabilized at room temperature when $x \geq 0.4$. Similar phenomenon that the rhombohedral distortion decreases with increasing BNiT content in NBT-BNiT solid solutions was also reported by Bai *et al.* [33]. The discrepancy between experimentally observed crystal structure and predicted structure by t has also been observed in other NBT-based solid solutions. For example, in NBT-$BiMg_{0.5}Ti_{0.5}O_3$ (NBT-BMgT) solid solutions, although incorporation of the large Mg^{2+} ions ($r(Mg^{2+})$ = 0.72 Å, 6-fold coordinated) results in a reduction in t, XRD patterns show the rhombohedral superlattice peak begins to disappear when the mole fraction of BMgT reaches 4~5%. The crystal symmetry tends to become pseudo-cubic or cubic with further increase in the mole fraction of BMgT to 6~50% [49-51]. The above observations seem to contradict the empirical prediction that a high symmetry phase (tetragonal or cubic) is formed when $t \sim 1$.

XPS results for Ni 2p (Fig.6e and Table 2) show the presence of Ni^{3+} in the NBT-BNiT solid solutions,

which is further supported by the existence of *p*-type electronic conduction behaviour revealed by impedance measurements under different atmospheres (Fig.9). As will be discussed later, Ni^{3+} is considered as the main species for hole location to give rise to *p*-type electronic conduction. In NiO_6 octahedra, Ni^{3+} is also in the low-spin state [23] with ionic radius of $r(Ni^{3+}$, 6-fold, low-spin) = 0.56 Å [24], which is much smaller than that of Ni^{2+}. According to the estimated Ni^{3+} fraction in Table 2, assuming 50% Ni^{2+} ions in the NBT-BNiT solid solutions are oxidised to Ni^{3+}, the tolerance factor *t* decreases linearly with increasing *x* from 0.9841 for NBT to 0.9823 for $x = 0.6$. This fails to explain the transition from rhombohedral to pseudo-cubic symmetry with increasing BNiT content in the solid solutions. Moreover, even if all the Ni^{2+} ions are oxidised to Ni^{3+}, the largest *t* (0.9908) is obtained at $x = 0.6$, which is not high enough to stabilise the tetragonal phase. For example, in $(Na_{1-x}K_x)_{0.5}Bi_{0.5}TiO_3$ (NKBT) series, tetragonal phase is observed only when $x \geq 0.8$ with $t \geq 1.019$ [52]. Alternative reasons have to be considered to explain the coexistence of rhombohedral and tetragonal phases when $x \geq 0.4$.

To understand the stabilisation mechanism for the tetragonal phase in the NBT-BNiT solid solutions, the weighed and ball-milled powders for $x = 0.6$ were calcined at different temperatures. XRD patterns (Fig.11a) show that the calcined powders contain $Na_{0.5}Bi_{4.5}Ti_4O_{15}$ (NBiT) as a predominant secondary phase, which is not observed during calcination of NBT [53]. The peak intensity for NBiT decreases with increasing calcination temperature, and disappears after sintering at 1100 °C. This indicates that a partial perovskite structure is converted from the Aurivillius structure of NBiT after sintering. NBiT is also the precursor for synthesizing a textured NBT using the template grain growth (TGG) or topochemical microcrystal conversion (TMC) method [54-57], where anisotropic NBiT platelets were obtained using molten salt synthesis sintered at 1050 ~ 1100 ℃ prior to the conversion of NBT obtained from the mixture of NBiT, Na_2CO_3 and TiO_2 using molten salt synthesis samples sintered at 950 ~ 1100 ℃. The preferred orientation of particle growth for the NBT prepared by the TMC method and the conventional solid-state synthesis were [100]p and [110]p, respectively [57]. Fig.11b shows the compositional dependence of the relative intensity for the (100)p peak, which was calculated by $I(100)_p/\sum I_i$ from the XRD patterns in Fig.1. The relative intensity of the $(100)_p$ increases almost linearly with *x*, indicating a preference of orientation may possibly occur. Several points are in common for the conversion of perovskite NBT between the solid-state synthesis of BNiT-NBT and the TGG/TMC method: (1) BNiT as the template, (2) similar reaction temperatures, and (3) preferred orientation [100]p. Therefore, the tetragonal phase may be stabilised by BNiT because the perovskite NBT converted from the NBiT templates has a preferred orientation.

It is worth mentioning that the room temperature ND patterns in Fig.3 confirm coexistence of the rhombohedral phase with $a^-a^-a^-$ tilting and the tetragonal phase with $a^0a^0a^+$ tilting for $x \geq 0.4$. Coexistence of two phases with different tilting systems was also observed at 300 °C for NBT by ND studies [36]. Some nanometre-scale tetragonal platelets with preferred orientation along {100} were found at room temperature by TEM studies [58-60], where Beanland and Thomas [59] showed that they were with $a^0a^0a^+$ tilting embedded in the rhombohedral $a^-a^-a^-$ matrix. They also indicated that these tetragonal platelets acted strongly to impede domain wall motion, and thus T_m occurred during the phase transition from the rhombohedral to tetragonal phase. Based on the LCR results shown in Fig.8, T_m increases from 323 to 342 °C when the average structure is dominated by the rhombohedral phase at room temperature for $x \leq 0.2$. In contrast, the presence of a tetragonal phase at room temperature for $x \geq 0.4$ leads to a decrease in T_m in conjunction with peak flattening. As a reduction of T_m is also observed for $x = 0.3$, it is possible phase co-existence may also occur for $x = 0.3$. Further TEM studies may be required to clarify the hypothesis.

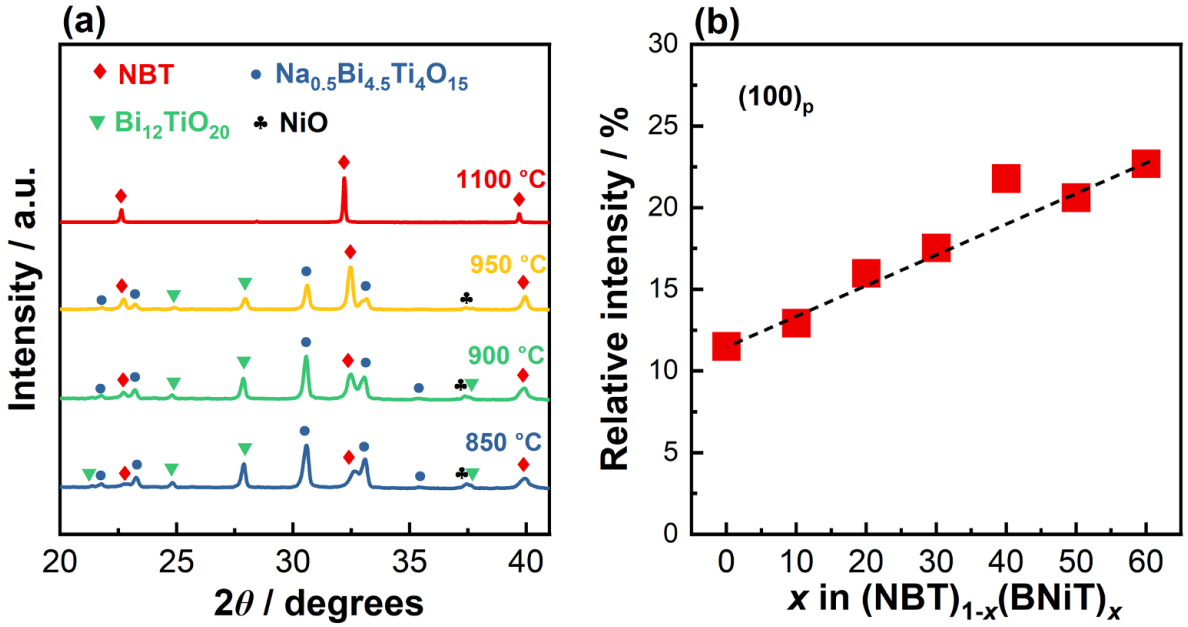

Figure 11. (a) Room-temperature XRD patterns for $x = 0.6$ calcined at different temperatures. (b) Compositional dependence of the relative intensity for the (100)p peak in the solid solutions.

4.2 Defect chemistry and electrical conductivity

As revealed by our previous studies, the defect chemistry for NBT can be best described by an ionic compensation mechanism according to the following defect equation

$$2Bi_{Bi}^{2} + 3O_O^x \xrightarrow{-Bi_2O_3} 2V_{Bi}''' + 3V_O^{\cdot\cdot} \quad (2)$$

where oxygen vacancies are created by Bi_2O_3 loss during ceramic processing to facilitate oxide-ion conduction in NBT. Partial reduction of Ti^{4+} to Ti^{3+} caused by oxygen loss at high temperatures and reoxidation of Ti^{3+} to Ti^{4+} caused by oxygen regain during furnace-cooling are not considered as the oxidation state of Ti in NBT remains +4, which is supported by the absence any *n*-type electronic conduction in addition to XPS analysis. Oxidation of O^{2-} to O^- during cooling, as described by

$$O_O^x + V_O^{\cdot\cdot} + \frac{1}{2}O_2(g) \rightarrow 2O_O^{\cdot} \quad (3)$$

can be also excluded as no *p*-type electronic conduction behavior is observed for NBT.

To form NBT-BNiT solid solutions, the charge compensation mechanism can be described by the following equation:

$$Bi_2O_3 + 2NiO + 2Na_{Na}^x + 2Ti_{Ti}^x \rightarrow 2Bi_{Na}^{\cdot\cdot} + 2Ni_{Ti}'' + Na_2O + 2TiO_2 \quad (4)$$

where acceptor doping on the B-site (partial replacement of Ti^{4+} by Ni^{2+}) is compensated by donor doping on the A-site (partial replacement of Na^+ by Bi^{3+}). Here the oxidation state of Ni is assumed to be +2 as NiO was used as the starting material for Ni source. For each Ni acceptor dopant for Ti on the B-site, it requires one Bi donor dopant for Na on the A-site. This mechanism does not involve any change in oxygen stoichiometry, and thus can be considered as a 'stoichiometric' mechanism. During cooling, uptake of oxygen may partially oxidise Ni^{2+} to Ni^{3+}according to

$$2Ni_{Ni}^x + V_O^{\cdot\cdot} + \frac{1}{2}O_2(g) \rightarrow 2Ni_{Ni}^{\cdot} + O_O^x \quad (5)$$

This will give rise to *p*-type electronic conduction. Furthermore, trapping of oxygen vacancies by the negatively charged acceptor dopants on the B-site can occur according to

$$V_O^{\cdot\cdot} + Ni_{Ti}'' \rightarrow (V_O^{\cdot\cdot} \cdot Ni_{Ti}'')^x \quad (6)$$

This will significantly decrease the mobility of oxygen vacancies to suppress the oxide-ion conductivity. At high temperatures, dissociation of the defect cluster may occur to release the trapped oxygen vacancies, as described by

$$(V_O^{\cdot\cdot} \cdot Ni_{Ti}'')^x \rightarrow V_O^{\cdot\cdot} + Ni_{Ti}'' \quad (7)$$

Based on the electrical properties of the NBT-BNiT solid solutions, the defect mechanism can be described by Equations (2), (5), (6) and (7) due to the following experimental evidences. (1) The presence of *p*-type electronic conduction in the NBT-BNiT solid solutions, as revealed by the impedance spectra in different atmospheres in Fig.9a-9c, supports the defect mechanism in Equation (4); (2) EMF transport number results show that all compositions have significant t_{ion} (~ 10-20%) at 800 °C, indicating the presence of oxygen vacancies described by Equation (1). (3) t_{ion} values for $x \geq 0.2$ increase with increasing temperature from 600 to 800 °C, which is different from the t_{ion}-

temperature relationship of the predominantly ionic conducting NBT. An increased t_{ion} with temperature indicates that the trapped oxygen vacancies are released from the defect associates as described by Equation (6), which is similar to that observed in the classic oxide-ion conductor yttria-stabilised zirconia (YSZ).

Based on the above defect chemistry analysis, the observed "V-shape" conductivity-composition relationship of the NBT-BNiT series can be attributed to a competition between the suppressed ionic component due to trapping of oxygen vacancies and the enhanced electronic component due to an increase in the Ni content on the B-site, as shown in Fig.12. First, the variation of the ionic component with increasing BNiT content is considered. As shown by our previous study [27], Al^{3+} with a small ionic radius ($r(Al^{3+})$ = 0.535 Å, 6-fold coordinated) has a strong ability to trap oxygen vacancies that 7% Al^{3+} can fully eliminate the oxide-ion conduction in NBT-BA solid solutions. Thus, the NBT-BA is considered as a representative system where strong trapping between the B-site acceptor dopants and oxygen vacancies exists. The conductivity-composition relationship of such system is described by Line 1. On the contrary, Sc^{3+} with a large ionic radius ($r(Sc^{3+})$ = 0.745 Å, 6-fold coordinated) has a weak ability to trap oxygen vacancies, and thus the NBT-BS series is considered as a model system for weak trapping. Conductivity of the NBT-BS series decreases slowly with increasing BS content following Line 2. In an ideal case without any trapping, the ionic conductivity remains constant, as described by Line 3. Therefore, Line 1, 2 and 3 represent the compositional dependence of the ionic conductivity for strong trapping, weak trapping and no trapping systems, respectively. Second, the variation of the electronic component with increasing BNiT content is evaluated. As shown in Fig.9d, t_{ion} values for x = 0.4 and 0.6 approach zero at 600 °C, suggesting the electrical conductivity is predominated by electronic conduction. In Fig.12, the electrical conductivity (in log scale) varies linearly with x when $0.4 \leq x \leq 0.6$. Extrapolation of the linear relationship to x = 0 shows that the conductivity agrees with the value for $NB_{0.51}T$, which presents a predominant electronic conduction behaviour [1, 45]. Therefore, if no oxide ion conduction is involved, the electronic conductivity increases linearly with increasing x following Line 4. The mixed conductivity for strong, weak and no trapping systems can be calculated by Line 5 = Line 1 + Line 4, Line 6 = Line 2 + Line 4 and Line 7 = Line 3 + Line 4, respectively. Line 5 and Line 7 represent the lower and the upper limit for the mixed conductivity in the solid solutions. The experimentally observed conductivity-composition relationship is close to Line 6, suggesting the oxygen vacancies are weakly trapped by Ni.

As also shown in Fig.12, the highest electrical conductivity achieved in NBT-BNiT solid solutions is

slightly higher that obtained in NBT-BC solid solutions albeit BNiT has a much large solid solution limit in NBT than BC. Therefore, incorporation of BNiT may not be good for developing NBT-based mixed conductors, however, it is effective to reduce the dielectric loss when the BNiT content ≤ 40%.

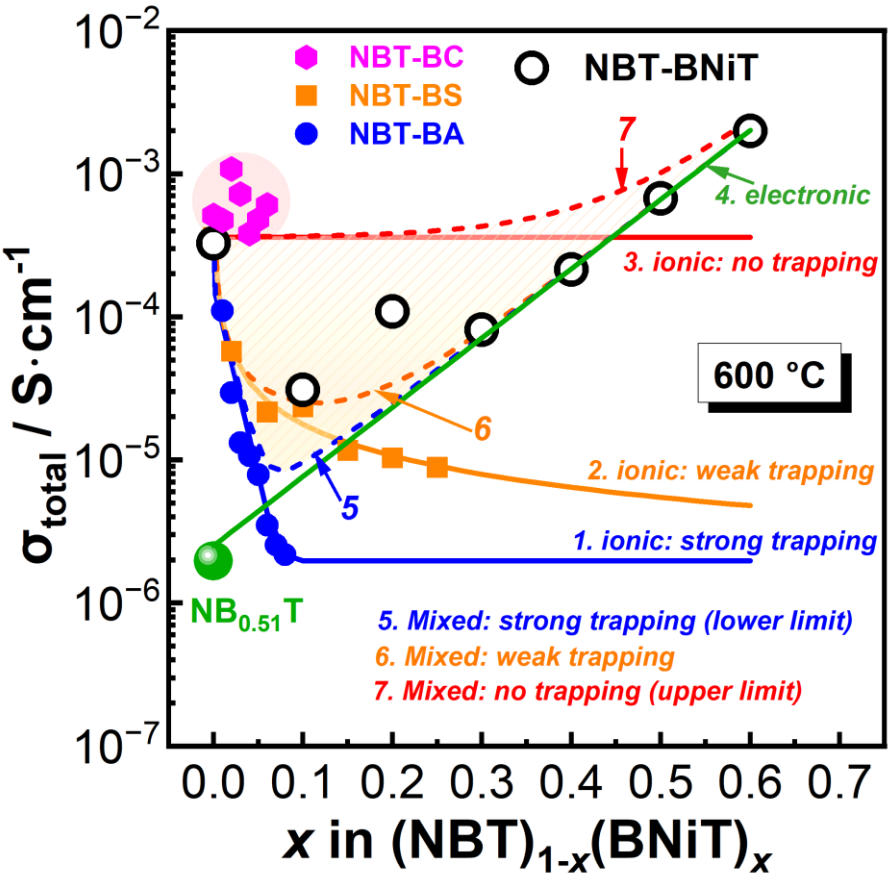

Figure 12. Compositional dependence of the total conductivity of the NBT-BNiT series in comparison with NBT-BA [27], NBT-BS [28] and NBT-BC [22] solid solutions. Data for $NB_{0.51}T$ is from Ref. [45].

5. Conclusion

Solid solutions of NBT and BNiT were prepared by the solid-state reaction method and their electrical properties were investigated to explore the possibility of obtaining high level of mixed ionic-electronic conductivity by incorporating a large amount of transition metal ions onto the B-site of NBT. Phase evolution of the solid solutions with varying compositions was also investigated by neutron diffraction studies. The results show that incorporation of BNiT into NBT has a dramatic impact on its crystal structure and electrical conduction mechanism. Major conclusions are summarized below.

(1) The solid solution limit of BNiT in NBT is 60% based on XRD, and therefore up to 30% of

Ni can be introduced onto the B-site of the perovskite. With increasing BNiT content in the solid solutions, the crystal structure changes from rhombohedral to pseudo-cubic.

(2) Coexistence of rhombohedral and tetragonal phases was identified by neutron diffraction for $x \geq 40\%$. Stabilisation of the tetragonal phase may possibly be related to the conversion of the perovskite NBT from the Aurivillius NBiT during solid state reaction. Phase coexistence leads to peak broadening on the permittivity-temperature profile and a decrease of T_m to ~200 °C.

(3) The total electrical conductivity shows a V-shape variation with increasing x and the conduction mechanism changes from predominant oxide-ion conduction for NBT, mixed ionic-electronic conduction for $x = 20\%$, to predominant p-type electronic conduction for $x \geq 40\%$. The observed conductivity-composition relationship originates from a competing effect between the suppressed oxide-ion conduction due to oxygen ion trapping and the enhanced electronic conduction due to hole hopping between Ni^{2+} (Ni_{Ni}^{x}) and Ni^{3+} ($Ni_{Ni}^{\cdot}$).

(4) Although NBiT has a large solid solution limit in NBT, high mixed ionic-electronic conductivity is not obtained. Incorporation of BNiT may not be good for developing NBT-based mixed conductors, however, it is effective to reduce the dielectric loss to benefit dielectric applications when the BNiT content ≤ 40%.

Acknowledgements

The authors thank National Natural Science Foundation of China (52072239, 52234010), and EPSRC (EP/L027348/1) for funding this project. We acknowledged The Instrumental Analysis Center of Shanghai Jiao Tong University for providing XPS analysis.

Declaration of Competing Interest

The authors declare that they have no known competing financial interests or personal relationships that could have appeared to influence the work reported in this paper.

Reference

[1] M. Li, M. J. Pietrowski, R. A. De Souza, H. Zhang, I. M. Reaney, S. N. Cook, J. A. Kilner and D. C. Sinclair, "A family of oxide-ion conductors based on the ferroelectric perovskite $Na_{0.5}Bi_{0.5}TiO_3$", Nature Materials 31 (2014) 31-35.

[2] M. Li, H. Zhang, S. N. Cook, L. Li, J. Kilner, I. M. Reaney and D. C. Sinclair, "Dramatic influence of A-site nonstoichiometry on the electrical conductivity and conduction mechanisms in the perovskite oxide $Na_{0.5}Bi_{0.5}TiO_3$", Chemistry of Materials 27 (2015) 629-634.

[3] X. Chen, J. Zeng, X. Yan, M. Zhou, P. Tang, T. Liang and W. Li, "Effects of Bi deficiency on the microstructural and conductive properties of $Na_{0.5}Bi_{0.5}TiO_3$ (NBT) perovskite", Solid State Ionics 209 (2017) 152-162.

[4] X. Chen, M. Zhou, J. Shi, T. Liang, J. Zeng, X. Yan, N. Luo, W. Li and Y. Wei, "Microstructure and electrical conductivity of A-site fully stoichiometric $Na_{0.5+x}Bi_{0.5-x}TiO_{3-\delta}$ with different Na/Bi ratios", Ceramics International 45 (2019) 11438-11447.

[5] J. Shi, X. Liu, F. Zhu, W. Tian, Y. Xia, T. Li, R. Rao, T. Zhang, L. Liu, "Oxygen vacancy migration and its lattice structural origin in A-site non-stoichiometric bismuth sodium titanate perovskites", Journal of Materiomics 8 (2022) 719-729.

[6] F. Yang, M. Li, L. Li, P. Wu, E. Pradal-Velázquez and D. C. Sinclair, "Optimisation of oxide-ion conductivity in acceptor-doped $Na_{0.5}Bi_{0.5}TiO_3$ perovskite: approaching the limit?", Journal of Materials Chemistry A 5 (2017) 21658-21662.

[7] F. Yang, Y. Hu, Q. Hu, P. Wu and D. C. Sinclair, "Electrical and dielectric properties of Ca-doped Bi-deficient sodium bismuth titanate $Na_{0.5}Bi_{0.49-x}Ca_xTiO_{3-\delta}$ $(0 \le x \le 0.08)$", Crystals 12 (2022) 1800.

[8] F. Yang, P. Wu and D. C. Sinclair, "Enhanced bulk conductivity of A-site divalent acceptor-doped non-stoichiometric sodium bismuth titanate", Solid State Ionics 299 (2017) 38-45.

[9] F. Yang, H. Zhang, L. Li, I. M. Reaney and D. C. Sinclair, "High ionic conductivity with low degradation in A-site strontium-doped nonstoichiometric sodium bismuth titanate perovskite", Chemistry of Materials 28 (2016) 5269-5273.

[10] D. P. C. Shih, A. Aguadero and S. J. Skinner, "Improvement of ionic conductivity in A-site lithium doped sodium bismuth titanate", Solid State Ionics 317 (2018) 32-38.

[11] D. P. C. Shih, A. Aguadero and S. J. Skinner, "A-site acceptor-doping strategy to enhance oxygen transport in sodium-bismuth-titanate perovskite", Journal of the American Ceramic Society 106 (2023) 100-108.

[12] L. Koch, S. Steiner, K. Meyer, I. Seo, K. Albe and T. Frömling, "Ionic conductivity of acceptor doped sodium bismuth titanate: influence of dopants, phase transitions and defect associates", Journal of Materials Chemistry C 5 (2017) 8958-8965.

[13] R. Bhattacharyya, S. Das and S. Omar, "High ionic conductivity of Mg^{2+}-doped non-stoichiometric sodium bismuth titanate", Acta Materialia 159 (2018) 8-15.

[14] Y. Lu, C. A. López, J. Wang, J. A. Alonso and C. Sun, "Insight into the structure and functional application of Mg-doped $Na_{0.5}Bi_{0.5}TiO_3$ electrolyte for solid oxide fuel cells", Journal of Alloys and Compounds 752 (2018) 213-219.

[15] P. Singh, R. Pandey and P. Singh, "Polyol-mediated synthesis of Bi-deficient Mg^{2+}-doped sodium bismuth titanate and study of oxide ion migration behavior with functional properties", Journal of Alloys and Compounds 860 (2021) 158492.

[16] R. Bhattacharyya and S. Omar, "Electrical conductivity study of B-site Ga doped non-stoichiometric sodium bismuth titanate ceramics", Journal of Alloys and Compounds 746 (2018) 54-61.

[17] M. Y. Li, C. He, W. G. Wang, G. L. Hao, X. Y. Li, T. Liu, X. F. Wang and D. Wang, "Investigation of Ga doping for non-stoichiometric sodium bismuth titanate ceramics", Journal of Materials Science: Materials in Electronics 32 (2021) 16140-16112.

[18] S. Steiner, I. Seo, P. Ren, M. Li, D. J. Keeble and T. Frömling, "The effect of Fe-acceptor doping on the electrical properties of $Na_{1/2}Bi_{1/2}TiO_3$ and $0.94(Na_{1/2}Bi_{1/2})TiO_3$-$0.06BaTiO_3$", Journal of the American Ceramic Society 102 (2019) 5295-5304.

[19] P. B. Groszewicz, L. Koch, S. Steiner, A. Ayrikyan, K. G. Webber, T. Frömling, K. Albe and G. Buntkowsky, "The fate of aluminium in (Na,Bi)TiO_3-based ionic conductors", Journal of Materials Chemistry A 8 (2020) 18188-18197.

[20] L. Koch, S. Steiner, A. Hoang, A. J. Klomp, K. Albe and T. Frömling, "Revealing the impact of acceptor dopant type on the electrical conductivity of sodium bismuth titanate", Acta Materialia 229 (2022) 117808.

[21] R. A. De Souza, "Oxygen diffusion in $SrTiO_3$ and related perovskite oxides", Advanced Functional Materials 25 (2015) 6326-6342.

[22] F. Yang, Y. Du, Y. Hu, Q. Hu, P. Wu and D. C. Sinclair, "Mixed ionic-electronic conduction and defect chemistry of $(Na_{0.5}Bi_{0.5}TiO_3)_{1-x}(BiCoO_3)_x$ ($0 \leq x \leq 0.06$) solid solutions", Journal of Materials Chemistry A 11 (2023) 16159-16171.

[23] Q. Hu, Y. Xue, J. Kang, I. Scivetti, G. Teobaldi, A. Selloni, L. Guo and L. Liu, "Structure and oxygen evolution activity of β-NiOOH: where are the protons?", ACS Catalysis 12 (2022) 295-304.

[24] R. D. Shannon, "Revised effective ionic radii and systematic studies of interatomic distances in halides and chalcogenides", Acta Crystallographica Section A 31 (1976) 751-767.

[25] W. T. Hong, M. Risch, K. A. Stoerzinger, A. Grimaud, J. Suntivich and Y. Shao-Horn, "Toward the rational design of non-precious transition metal oxides for oxygen electrocatalysis", Energy & Environmental Science 8 (2015) 1404-1427.

[26] J. Hwang, R. Rao, L. Giordano, Y. Katayama, Y. Yu and Y. Shao-Horn, "Peroskites in catalysis and electrocatalysis", Science 358 (2017) 751-756.

[27] F. Yang, P. Wu, D. C. Sinclair. Suppression of electrical conductivity and switching of conduction mechanisms in 'stoichiometric' $(Na_{0.5}Bi_{0.5}TiO_3)_{1-x}(BiAlO_3)x$ ($0 \leq x \leq 0.08$) solid solutions, Journal of Materials Chemistry C 5 (2017) 7243-7252.

[28] F. Yang, P. Wu, D. C. Sinclair. Electrical conductivity and conduction mechanisms in $(Na_{0.5}Bi_{0.5}TiO_3)_{1-x}(BiScO_3)_x$ ($0.00 \leq x \leq 0.25$) solid solutions, Journal of Materials Chemistry C 6 (2018) 11598-11607.

[29] Y. Inaguma and T. Katsumata, "High pressure synthesis, lattice distortion, and dielectric properties of a perovskite $Bi(Ni_{1/2}Ti_{1/2})O_3$", Ferroelectrics 286 (2003) 111-117.

[30] J. Zhu, S. Feng, Q. Liu, J. Zhang, H. Xu, Y. Li, X. Li, J. Liu, Q. Huang, Y. Zhao and C. Jin, "Temperature and pressure effects of multiferroic Bi_2NiTiO_6 compound", Journal of Applied Physics 113 (2013) 143514.

[31] S. M. Choi, C. J. Stringer, T. R. Shrout and C. A. Randall, "Structure and property investigation of a Bi-based perovskite solid solution: (1-x) $Bi(Ni_{1/2}Ti_{1/2})O_3$-$x$$PbTiO_3$", Journal of Applied Physics 98 (2005) 034108.

[32] I. Fuji, K. Nakashima, N. Kumada and S. Wada, "Structural, dielectric, and piezoelectric properties of $BaTiO_3$- $Bi(Ni_{1/2}Ti_{1/2})O_3$ ceramics", Journal of the Ceramic Society of Japan 120 (2012) 30-34.

[33] W. Bai, F. Liu, P. Li, B. shen, J. Zhai and H. Chen, "Structure and electromechanical properties in $Bi_{0.5}Na_{0.5}TiO_3$-based lead-free piezoceramics with calculated end-member $Bi(Ni_{0.5}Ti_{0.5})O_3$", Journal of the European Ceramic Society 35 (2015) 3457-3466.

[34] A. C. Larson and R. B. Von Drelle, General Structure Analysis System (GSAS), Los Alamos National Laboratory Report LAUR, 1994, pp. 76-748.

[35] B. H. Toby, "EXPGUI, a graphical user interface for GSAS", Journal of Applied Crystallography, 34 (2001) 210-213.

[36] G. O. Jones and P. A. Thomas, "Investigation of the structure and phase transitions in the novel A-site substituted distorted perovskite compound $Na_{0.5}Bi_{0.5}TiO_3$", Acta Crystallographica Section B 58 (2002) 168-178.

[37] J. Miao, L. Li, H. Liu, D. Xu, Z. Lu, Y. Song, W. Su and Y. Zheng, "Structure characteristics and valence state study for $La_{1-x}Na_xTiO_3$ synthesized under high-pressure and high-temperature conditions", Materials Letters 42 (2000) 1-6.

[38] S. Mahboob, G. Prasad, C. Chou and S. G. Kumar, "Electrical and X-ray photoelectron spectroscopy study on $(Na_{0.5-x}K_xBi_{0.5-x}Nd_x)TiO_3$ Ceramics", Ferroelectrics 445 (2013) 161-171.

[39] N. Dai, J. Feng, Z. Wang, T. Jiang, W. Sun, J. Qiao and K. Sun, "Synthesis and characterization of B-site Ni-doped perovskites $Sr_2Fe_{1.5-x}Ni_xMo_{0.5}O_{6-\delta}$ (x = 0, 0.05, 0.1, 0.2, 0.4) as cathodes for SOFCs", Journal of Materials Chemistry A 1 (2013) 14147-14153.

[40] X. Xu, Y. Chen, W. Zhou, Z. Zhu, C. Su, M. Liu and Z. Shao, "A perovskite electrocatalyst for efficient hydrogen evolution reaction", Advanced Materials 28 (2016) 6442-6448.

[41] O. Bondarchuk, A. P. LaGrow, A. Kvasha, T. Thieu, E. Ayerbe and I. Urdampilleta, "On the X-ray photoelectron spectroscopy analysis of $LiNi_xMn_yCo_zO_2$ material and electrodes", Applied Surface Science 535 (2021) 147699.

[42] J. T. S. Irvine, D. C. Sinclair and A. R. West, "Electroceramics: characterization by impedance spectroscopy", Advanced Materials 2 (1990) 132-138.

[43] J. Fleig, "The grain boundary impedance of random microstructures: Numerical simulations and implications for the analysis of experimental data", Solid State Ionics 150 (2002) 181-193.

[44] F. Yang, M. Li, L. Li, P. Wu, E. Pradal-Velázquez, D. C. Sinclair. Defect chemistry and electrical properties of $Na_{0.5}Bi_{0.5}TiO_3$ perovskite, Journal of Materials Chemistry A 6 (2018) 5241-5242.

[45] F. Yang, J. S. Dean, Q. Hu, P. Wu, E. Pradal-Velázquez, L. Li and D. C. Sinclair, "From insulator to oxide-ion conductor by a synergistic effect from defect chemistry and microstructure: acceptor-doped Bi-excess sodium bismuth titanate $Na_{0.5}Bi_{0.51}TiO_{3.015}$", Journal of Materials Chemistry A 8 (2020) 25120-25130.

[46] J. Zhao, J. Gao, W. Li, Y. Qian, X. Shen, X. Wang, X. Shen, Z. Hu, C. Dong, Q. Huang, L. Cao, Z. Li, J. Zhang, C. Ren, L. Duan, Q. Liu, R. Yu, Y. Ren, S. Weng, H. Lin, C. Chen, L. Tjeng, Y. Long, Z. Deng, J. Zhu, X. Wang, H. Weng, R. Yu, M. Greenblatt and C. Jin, "A combinatory ferroelectric compound bridging simple ABO_3 and A-site-ordered quadruple perovskite", Nature Communications 12 (2021) 747.

[47] S. Qin, Y. Chin, B. Zhou, Z. Liu, X. Ye, J. Guo, G. Liu, C. Chen, Z. Hu and Y. Long, "High-pressure synthesis and magnetism of the 4H-$BaMnO_3$ single crystal and its 6H-type polymorph", Inorganic Chemistry 60 (2021) 16308-16315.

[48] A. S. Bhalla, R. Guo and R. Roy, "The perovskite structure-a review of its role in ceramic science and technology", Materials Research Innovations 4 (2000) 3-26.

[49] Q. Wang, J. Chen, L. Fan, L. Liu, L. Fang and X. Xing, "Preparation and electric properties of $Bi_{0.5}Na_{0.5}TiO_3$-$Bi(Mg_{0.5}Ti_{0.5})O_3$ lead-free piezoceramics", Journal of the American Ceramic Society 96 (2013) 1171-1175.

[50] D. E. Jain Ruth, M. Muneeswaran, N. V. Giridharan and B. Sundarakannan, "Structural and electrical properties of bismuth magnesium titanate substituted lead-free sodium bismuth titanate ceramics", Journal of Materials Science: Materials in Electronics 27 (2016) 7018-7023.

[51] X. Wang and W. Cao, "Dielectric properties of new perovskite ceramics $(Na_{1/4}Bi_{3/4})(Mg_{1/4}Ti_{3/4})O_3$ and $(K_{1/4}Bi_{3/4})(Mg_{1/4}Ti_{3/4})O_3$", Journal of the European Ceramic Society 27 (2007) 2481-2484.

[52] G. O. Jones, J. Kreisel and P. A. Thomas, "A structural study of the $(Na_{1-x}K_x)_{0.5}Bi_{0.5}TiO_3$ perovskite series as a function of substitution (x) and temperature", Powder Diffraction 17 (2002) 301-309.

[53] F. Yang, Y. Hu, Q. Hu, S. Steiner, T. Frömling, L. Li, P. Wu, E. Pradal-Velázquez and D. C. Sinclair, "Dramatic impact of the TiO_2 polymorph on the electrical properties of 'stoichiometric' $Na_{0.5}Bi_{0.5}TiO_3$ ceramics prepared by solid-state reaction", Journal of Materials Chemistry A 10 (2022) 891-901.

[54] P. Setasuwon and S. Kijamnajsuk, "Synthesis of $Na_{0.5}Bi_{0.5}TiO_3$ anisotropic particles with grain orientation by conversion of $Na_{0.5}Bi_{4.5}Ti_4O_{15}$ crystals", Science and Technology of Advanced Materials 7 (2006) 780-784.

[55] J. T. Zeng, K. W. Kwok, W. K. Tam, H. Y. Tian, X. P. Jiang and H. L. W. Chan, "Plate-like $Na_{0.5}Bi_{0.5}TiO_3$ template synthesized by a topochemical method", Journal of the American Ceramic Society 89 (2006) 3850-3853.

[56] C. Jiang, K. Zhou, X. Zhou, Z. Li and D. Zhang, "Synthesis and characterization of $Na_{0.5}Bi_{0.5}TiO_3$ platelets with preferred orientation using Aurivillius precursors", Ceramics International 41 (2015) 6858-6862.

[57] A. Hussain, J. U. Rahman, F. Ahemd, J. Kim, M. Kim, T. Song and W. Kim, "Plate-like $Na_{0.5}Bi_{0.5}TiO_3$ particles synthesized by topochemical microcrystal conversion method", Journal of the European Ceramic Society 35 (2015) 919-925.

[58] B. Dorcet and G. Trolliard, "A transmission electron microscopy study of the A-site disordered perovskite $Na_{0.5}Bi_{0.5}TiO_3$", Acta Materialia 56 (2008) 1753-1761.

[59] R. Beanland and P. A. Thomas, "Imaging planar tetragonal sheets in rhombohedral $Na_{0.5}Bi_{0.5}TiO_3$ using transmission electron microscopy", Scripta Materialia 65 (2011) 440-443.

[60] R. Beanland and P. A. Thomas, "Symmetry and defects in rhombohedral single-crystalline $Na_{0.5}Bi_{0.5}TiO_3$", Physical Review B 89 (2014) 174102.